LUND UNIVERSITY

Microscopic approach to second harmonic generation in quantum cascade lasers

Winge, David; Franckie, Martin; Wacker, Andreas

Link to publication

Microscopic approach to second harmonic generation in quantum cascade lasers

David O. Winge[*]**, Martin Lindskog and Andreas Wacker**

Mathematical Physics, Lund University, Box 118, 22100 Lund, Sweden

[*]*David.Winge@teorfys.lu.se*

Abstract: Second harmonic generation is analyzed from a microscopical point of view using a non-equilibrium Green's function formalism. Through this approach the complete on-state of the laser can be modeled and results are compared to experiment with good agreement. In addition, higher order current response is extracted from the calculations and together with waveguide properties, these currents provide the intensity of the second harmonic in the structure considered. This power is compared to experimental results, also with good agreement. Furthermore, our results, which contain all coherences in the system, allow to check the validity of common simplified expressions.

References and links

1. J. Faist, F. Capasso, D. L. Sivco, C. Sirtori, A. L. Hutchinson, and A. Y. Cho, "Quantum cascade laser," Science **264**, 553 (1994).
2. M. M. Fejer, S. J. B. Yoo, R. L. Byer, A. Harwit, and J. S. Harris, Jr., "Observation of extremely large quadratic susceptibility at $9.6 - 10.8\mu$m in electric-field-biased AlGaAs quantum wells," Phys. Rev. Lett. **62**, 1041–1044 (1989).
3. E. Rosencher, A. Fiore, B. Winter, V. Berger, P. Bois, and J. Nagle, "Quantum engineering of optical nonlinearities," Science **271**, 168–173 (1996).
4. F. Capasso, C. Sirtori, and A. Y. Cho, "Coupled quantum well semiconductors with giant electric field tunable nonlinear optical properties in the infrared," IEEE J. Quantum Electron. **30**, 1313–1326 (1994).
5. M. A. Belkin, F. Capasso, A. Belyanin, D. L. Sivco, A. Y. Cho, D. C. Oakley, C. J. Vineis, and G. W. Turner, "Terahertz quantum-cascade-laser source based on intracavity difference-frequency generation," Nat. Photonics **1**, 288–292 (2007).
6. N. Owschimikow, C. Gmachl, A. Belyanin, V. Kocharovsky, D. L. Sivco, R. Colombelli, F. Capasso, and A. Y. Cho, "Resonant second-order nonlinear optical processes in quantum cascade lasers," Phys. Rev. Lett. **90**, 043902 (2003).
7. J.-Y. Bengloan, A. De Rossi, V. Ortiz, X. Marcadet, M. Calligaro, I. Maurin, and C. Sirtori, "Intracavity sum-frequency generation in GaAs quantum cascade lasers," Appl. Phys. Lett. **84**, 2019–2021 (2004).
8. Y. Yao, J. A. Hoffman, and C. F. Gmachl, "Mid-infrared quantum cascade lasers," Nat. Photonics **6**, 432–439 (2012).
9. B. S. Williams, "Terahertz quantum-cascade lasers," Nat. Photonics **1**, 517 (2007).
10. A. Wacker, "Quantum cascade laser: An emerging technology," in *Nonlinear Laser Dynamics,* K. Lüdge, ed. (Wiley-VCH, 2011).
11. Y.-H. Cho and A. Belyanin, "Short-wavelength infrared second harmonic generation in quantum cascade lasers," J. Appl. Phys. **107**, 053116–053116–7 (2010).
12. J. Faist, F. Capasso, D. L. Sivco, A. L. Hutchinson, S.-N. G. Chu, and A. Y. Cho, "Short wavelength ($\lambda \sim 3.4\mu$m) quantum cascade laser based on strained compensated InGaAs/AlInAs," Appl. Phys. Lett. **72**, 680 (1998).

13. C. Gmachl, F. Capasso, D. L. Sivco, and A. Y. Cho, "Recent progress in quantum cascade lasers and applications," Rep. Prog. Phys. **64**, 1533 (2001).
14. F. Capasso, R. Paiella, R. Martini, R. Colombelli, C. Gmachl, T. Myers, M. S. Taubman, R. Williams, C. Bethea, K. Unterrainer, H. Y. Hwang, D. L. Sivco, A. Y. Cho, A. Sergent, H. Liu, and E. A. Whittaker, "Quantum cascade lasers: ultrahigh-speed operation, optical wireless communication, narrow linewidth, and far-infrared emission," IEEE J. Quantum Electron. **38**, 511–532 (2002).
15. C. Gmachl, A. Belyanin, D. L. Sivco, M. L. Peabody, N. Owschimikow, A. M. Sergent, F. Capasso, and A. Y. Cho, "Optimized second-harmonic generation in quantum cascade lasers," IEEE J. Quantum Electron. **39**, 1345–1355 (2003).
16. A. Wacker, M. Lindskog, and D. Winge, "Nonequilibrium green's function model for simulation of quantum cascade laser devices under operating conditions," IEEE J. Sel. Topics Quantum Electron. **99**, 1200611 (2013).
17. A. Gajić, J. Radovanović, V. Milanović, D. Indjin, and Z. Ikonić, "Genetic algorithm applied to the optimization of quantum cascade lasers with second harmonic generation," J. Appl. Phys. **115**, 053712 (2014).
18. J. Bai and D. Citrin, "Optical and transport characteristics of quantum-cascade lasers with optimized second-harmonic generation," IEEE J. Quantum Electron. **43**, 391–398 (2007).
19. F. Capasso, J. Faist, and C. Sirtori, "Mesoscopic phenomena in semiconductor nanostructures by quantum design," J. Math. Phys. **37**, 4775 (1996).
20. D. Indjin, P. Harrison, R. W. Kelsall, and Z. Ikonic, "Self-consistent scattering theory of transport and output characteristics of quantum cascade lasers," J. Appl. Phys. **91**, 9019 (2002).
21. A. Hugi, R. Maulini, and J. Faist, "External cavity quantum cascade laser," Semicond. Sci. Technol. **25**, 083001 (2010).
22. Y. Petitjean, F. Destic, J. Mollier, and C. Sirtori, "Dynamic modeling of terahertz quantum cascade lasers," IEEE J. Sel. Topics Quantum Electron. **17**, 22–29 (2011).
23. R. C. Iotti, E. Ciancio, and F. Rossi, "Quantum transport theory for semiconductor nanostructures: A density matrix formulation," Phys. Rev. B **72**, 125347 (2005).
24. R. Terazzi and J. Faist, "A density matrix model of transport and radiation in quantum cascade lasers," New J. Phys. **12**, 033045 (2010).
25. S. Kumar and Q. Hu, "Coherence of resonant-tunneling transport in terahertz quantum-cascade lasers," Phys. Rev. B **80**, 245316 (2009).
26. E. Dupont, S. Fathololoumi, and H. C. Liu, "Simplified density-matrix model applied to three-well terahertz quantum cascade lasers," Phys. Rev. B **81**, 205311 (2010).
27. R. C. Iotti and F. Rossi, "Nature of charge transport in quantum-cascade lasers," Phys. Rev. Lett. **87**, 146603 (2001).
28. H. Callebaut and Q. Hu, "Importance of coherence for electron transport in terahertz quantum cascade lasers," J. Appl. Phys. **98**, 104505 (2005).
29. C. Jirauschek and P. Lugli, "Monte-carlo-based spectral gain analysis for terahertz quantum cascade lasers," J. Appl. Phys. **105**, 123102 (2009).
30. S.-C. Lee and A. Wacker, "Nonequilibrium Green's function theory for transport and gain properties of quantum cascade structures," Phys. Rev. B **66**, 245314 (2002).
31. T. Kubis, C. Yeh, P. Vogl, A. Benz, G. Fasching, and C. Deutsch, "Theory of nonequilibrium quantum transport and energy dissipation in terahertz quantum cascade lasers," Phys. Rev. B **79**, 195323 (2009).
32. T. Schmielau and M. Pereira, "Nonequilibrium many body theory for quantum transport in terahertz quantum cascade lasers," Appl. Phys. Lett. **95**, 231111 (2009).
33. G. Haldaś and, A. Kolek, and I. Tralle, "Modeling of mid-infrared quantum cascade laser by means of nonequilibrium green's functions," IEEE J. Quantum Electron. **47**, 878 –885 (2011).
34. T. Brandes, "Truncation method for green's functions in time-dependent fields," Phys. Rev. B **56**, 1213 (1997).
35. H. Haug and S. Koch, *Quantum Theory of the Optical and Electronic Properties of Semiconductors* (World Scientific, 2009).
36. C. Sirtori, J. Faist, F. Capasso, D. L. Sivco, A. L. Hutchinson, and A. Y. Cho, "Quantum cascade laser with plasmon-enhanced waveguide operating at 8.4μm wavelength," Appl. Phys. Lett. **66**, 3242–3244 (1995).
37. D. O. Winge, M. Lindskog, and A. Wacker, "Nonlinear response of quantum cascade structures," Appl. Phys. Lett. **101**, 211113 (2012).
38. O. Malis, A. Belyanin, C. Gmachl, D. L. Sivco, M. L. Peabody, A. M. Sergent, and A. Y. Cho, "Improvement of second-harmonic generation in quantum-cascade lasers with true phase matching," Appl. Phys. Lett. **84**, 2721–2723 (2004).
39. M. Belkin, Q. J. Wang, C. Pflugl, A. Belyanin, S. Khanna, A. Davies, E. Linfield, and F. Capasso, "High-temperature operation of terahertz quantum cascade laser sources," IEEE J. Sel. Topics Quantum Electron. **15**, 952 (2009).
40. Y. R. Shen, *The Principles of Nonlinear Optics* (Wiley, 1984).
41. R. Boyd, *Nonlinear Optics* (Academic, 1992).
42. F. Banit, S.-C. Lee, A. Knorr, and A. Wacker, "Self-consistent theory of the gain linewidth for quantum cascade lasers," Appl. Phys. Lett. **86**, 041108 (2005).
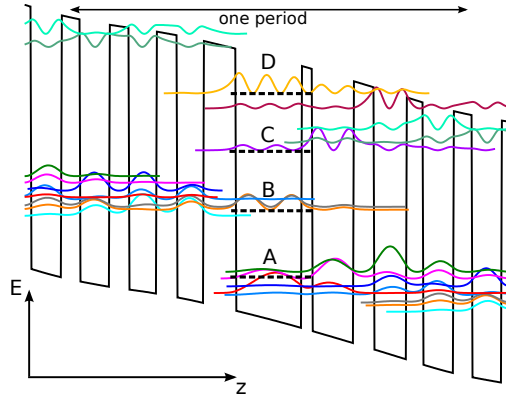
Fig. 1. One period of the structure from [15] with the two-well active region in the middle. Carriers are injected into the upper laser state B ensuring inversion between B and A, whereas levels A,C and B,D produce SH generation. The states and meanfield potential bending the conduction band structure are calculated at a bias drop of 190 mV per period. The period length d is 49.5 nm.

1. Introduction

The Quantum Cascade Laser [1] (QCL) consisting of hundreds of coupled quantum wells is well known to exhibit strong optical nonlinearities [2, 3] in particular in the infrared [4]. These nonlinearities have attracted much attention as they have proved a useful tool to achieve room-temperature terahertz sources through difference-frequency generation [5] and they can also be used the opposite way, extending the spectral range of the QCLs to lower wavelengths through Second Harmonic (SH) generation [6, 7].

Already today the QCL is widely used in many applications in both the mid-infrared [8] and the terahertz [9] spanning a wide range of frequencies [10]. However the fundamental frequency of a QCL is intrinsically limited by the conduction band offset as well as the energy level of the L-valley which effectively decreases laser performance when it is below the energy of the upper laser state [11]. The use of SH generation provides a way to circumvent these limitations. Among the reasons to extend the operation of QCLs beyond 3.5 μm [12] is the possibility to access strong spectral lines of important trace gases and also to use the quick modulation speed of QCLs compared to diode lasers [13, 14]. The latter could prove useful, if the wavelength could be compressed even further down towards the telecom region [11].

In structure D2912 considered by [15] a nonlinear resonator with high second order suscepti-bility is placed in the two central wells of the active region of the laser itself. The idea manifests itself in the ladder structure seen in Fig. 1. This allows for gain at the fundamental frequency and thus prevents saturation of the pump. The fact that the pump and the nonlinear resonator are integrated in the same heterostructure [6], provides us with the possibility to model the gen-eration of second harmonics with our non-equilibrium Green's function model for QCLs [16]. The same structure has recently been the subject of an optimization study centered at increas-ing the nonlinear conversion efficiency by Gajić *et al.* [17], as well as earlier by Bai *et al.* [18] where optimization was pursued by the use of supersymmetric mechanics and digitally graded heterostructures. The results in this work will be compared and evaluated partly in reference to these efforts.

2. The model

Simulations of quantum lasers are done on many different levels of complexity. Typically rate-equation based calculations [19, 20] are used as a starting point, where the simple treatment allows for a straightforward inclusion of additional effects as for example photon densities for dynamical simulations [21,22]. More advanced are density matrix methods were the coherences between different states are taken into account [23–26]. Monte-Carlo simulations are also used with the strong benefit that electron-electron scattering can be included at an early stage of implementation [27–29]. Finally, a full quantum treatment requires a solution of the two-time non-equilibrium Green's function (NEGF) [30–33], as is done in this work.

The two times of the Green's function contains the memory effects of the system. As an example, this gives rise to broadening of the levels due to their limited lifetimes. More importantly, it allows for a consistent treatment of the coherences in the system, as they also will be resolved in energy. This is problematic in for example density matrix approaches, where the energy of a coherence between two levels can not be clearly defined. The NEGF formalism solves this and thus extends further and beyond the semiconductor Bloch equations [35].

In our simulations we use a classical electromagnetic field. The field strength enters the model as $F(t) = F_{ac}\cos(\omega t)$ where ω is the driving field frequency and F_{ac} is the field amplitude. In the following we express the ac field strength as $eF_{ac}d$ in units of eV, where d is the period length. High intensities inside the QCL require a model going beyond linear response to the external electromagnetic field. This is done in our simulations by decomposing the time dependence of observables of the system in a Fourier series of the fundamental frequency ω and its higher harmonics. This procedure follows the concepts outlined in [34].

The scattering via impurities, interface roughness, alloy disorder as well as acoustic and optical phonons is contained in self-energies determined self-consistently. The phonons are assumed to follow a thermalized Boltzmann distribution, and this is the only place where the temperature enters the calculation. We use a lattice temperature of 100 K which is typically slightly higher than the heatsink temperature defined in experimental work [15]. Throughout these calculations the interface roughness was modeled by a exponential correlation function [16] with average island size and height of 10 nm and 0.1 nm respectively. The self-energies used are described in detail in [16] where we also show how solving for the Green's functions and projecting them down on to an ordinary density matrix gives access to observables such as the current density and occupations in different states.

Due to the time periodicity enforced on the system, the current response can be written as a Fourier series

$$J(t) = J_0 + \sum_{n=1}^{n_{max}} \left(J_n^{cos}\cos(n\omega t) + J_n^{sin}\sin(n\omega t) \right) \tag{1}$$

where J_0 is the stationary response and the J_n-terms are induced by the oscillating field. The *dynamical response* given by J_1^{cos} can be directly related to the gain coefficient after division by F_{ac}. In the same manner the J_2-terms can be seen as generators of second harmonics inside the waveguide of the structure considered.

For numerical reasons the value of n_{max} should be kept as low as possible as computational time increases by the square of the system size, which is linear in n_{max}. In practice this amounts to converging the calculations of the desired parameters with respect to n_{max} for a given ac field strength. Naturally convergence is more easily reached for observables involving terms related to $n = 1$ than those relying on terms with $n = 2$.
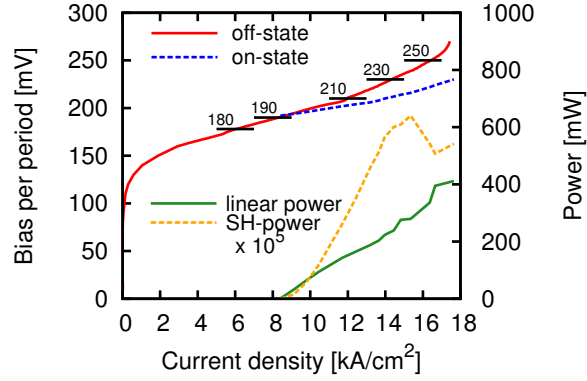
Fig. 2. Simulated bias-current relation of the structure studied for both the off- and on-state. The level of losses used to simulate the laser under operation was 40 cm^{-1}. Also shown is the output power at the pump and second harmonic frequency, respectively, using the TW model, which constitutes an upper bound. The second harmonic signal is scaled by a factor of 10^5. At the marked points 180, 190, 200, 210, 230 and 250 mV further analyses of gain and SH generation were carried out. A lattice temperature of 100 K was used.

3. Laser operation analysis

Calculations restricted by $n_{max} = 0$ provide the stationary response J_0 from Eq. (1). The oscillating electromagnetic field is thus not taken into account, giving the current density in the off-state of the laser, as shown in Fig. 2. Here, a number of bias points are marked indicating the points were more extensive analyses were made.

Gain is obtained through the dynamical response J_1^{cos} and thus accessible with $n_{max} = 1$. In Fig. 3, gain spectra as a function of photon energies are shown for the different bias points marked in Fig. 2. In the experiment of [15] a plasmon enhanced waveguide was used, similar to the one described in [36], where the overlap factor was calculated to be $\Gamma = 0.41$. Using reported waveguide loss from the experimental work, $\alpha_W = 15$ cm^{-1}, and by calculating the mirror loss from the reflectivity, $\alpha_M = 5.6$ cm^{-1}, the gain in the QCL structure required to compensate the losses is

$$g_{threshold} = \frac{\alpha_W + \alpha_M}{\Gamma}.$$

In this work the overlap factor is set to $\Gamma = 0.5$ following [18]. This enables easy comparison between results and yields the value $g_{threshold} = 40$ cm^{-1}. Studying Fig. 3, it can be seen that gain well above the level of the losses is reached for a large range of bias points. It can also be seen how the gain has a two-peak structure (e.g. 131 and 142 meV at $Fd = 210$ mV), where the lower energy transition becomes dominating with increasing bias. This indicates that the level structure is complex and that a crossing occurs at these bias points.

The gain spectra in Fig. 3 clearly show how the simulations predict the current threshold to be around 8 kA/cm^2, corresponding to 190 mV, for the design laser wavelength of 9.5 μm, or $\hbar\omega = 136.25$ meV. This value compares well to experiment, where a threshold current of 6.6 kA/cm^2 was reported. It can also be seen that the gain at the laser energy increases monotonically with bias, suggesting a steady increase in output power with bias. Provided that the nonlinear resonator in the active region is capable of sum frequency generation, conditions are thus fulfilled for observation of second harmonic generation in the structure. Experimental
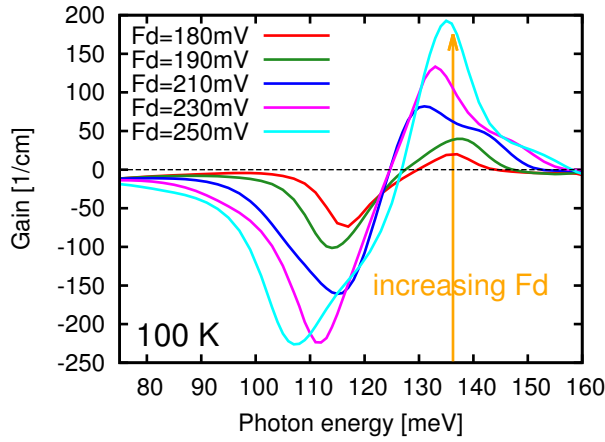
Fig. 3. Gain at weak ac field simulated at the bias points marked in Fig. 2. The orange arrow indicates the photon energy 136.25 meV corresponding to the fundamental wavelength of 9.5 μm, as well as increasing bias.
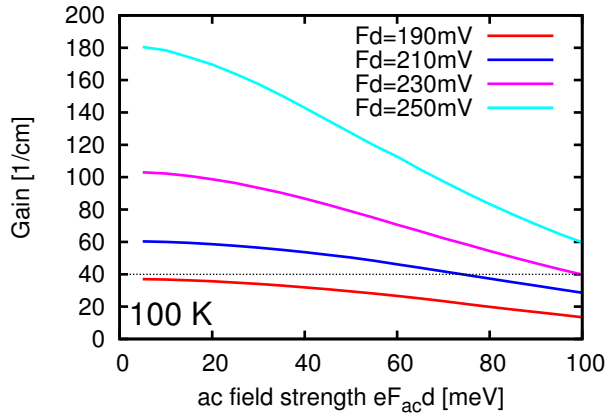

Fig. 4. Gain saturation with increasing ac field strength for the photon energy of 136.25 meV. The bias points examined are the ones indicated in Fig. 2. The ac field in the cavity increases as long as gain surpasses $g_{\text{threshold}}$ indicated as a dotted line.

measurements stop at 15 kA/cm^2, but it is clear from the simulations that gain persists even at higher bias points with higher currents.

By the use of a finite ac field strength in the simulations, the operation dynamics of the laser can be modeled as previously shown by our group in [37]. Increasing the ac field strength, the dynamical response J_1^{cos} increases sublinearly which leads to a saturation of the gain. This process can be studied in Fig. 4, again for the bias points indicated in Fig. 2. By increasing the ac field strength until gain reaches the level of the losses, the intensity at each bias point can be found, as well as the increase in current from Eq. (1) due to the stimulated emission.

In order to determine the optical power emitted by the laser, we proceed as follows: In the wave guide the electric field component $F_0\mathbf{e}_z\cos(k_\omega x - \omega t)$ is traveling towards the facet with an intensity given by the Pointing vector. Neglecting the intricate mode structure, we assume

a constant field over the active region of the waveguide. The corresponding facet area is given by 32.5 μm^2 from experimental data (#periods $\times$ d $\times$ waveguide width). Furthermore 71% is transmitted due to the Fresnel losses at the fundamental frequency. This provides the output power from our data, which is proportional to F_0^2.

Now, we have to relate F_0 to F_{ac} used in our simulation. If the electric field is dominated by the travelling wave (TW) $F_0 \mathbf{e}_z \cos(kx - \omega t)$, we can identify $F_0 = F_{ac}$ and the resulting power is shown in Fig. 2. On the other hand, there is a reflected wave, which is amplified and becomes of the same magnitude as the incoming wave further away from the facet. In the middle of the waveguide we have actually a standing wave (SW)

$$\mathbf{F}(x,t) = F_0 \mathbf{e}_z \cos(k_\omega x - \omega t) + F_0 \mathbf{e}_z \cos(k_\omega x + \omega t) = 2F_0 \cos(k_\omega x) \cos(\omega t) \mathbf{e}_z. \qquad (2)$$

As can be seen in Fig. 4 the gain saturation is roughly proportional to F_{ac}^2. Thus the spatial average $\langle \mathbf{F}^2(x,t) \rangle = 2F_0^2 \cos^2(\omega t)$ should be compared to the simulated $F_{ac}^2 \cos^2(\omega t)$, and we obtain $F_0 = F_{ac}/\sqrt{2}$, i.e. a reduction of output power with a factor of 2 compared to the TW case above.

Obviously, the TW and SW are extreme cases and the reality is in between. In addition, the z dependence of the electric field due to the mode profile will further complicate the situation. Thus, the TW and SW values should be taken as a confidence range for our results when we compare to experimental data in the following.

For a current density of 15 kA/cm^2, we find an output power of 280 mW for the TW case and 140 mW for the SW case. Here the experimental value is about 100 mW [15]. Taking into account, that the experimental collection efficiency is never unity and the Fresnel losses at the facet provide an upper bound for the transmission, we conclude that our results are in good agreement with the experimental data.

Finally, we compare the current simulations in the on-state with theoretical results obtained by Gajić *et al.* [17] and Bai *et al.* [18] who used a photon density equation coupled to the electron rate equations. Bai *et al.* finds an on-state current that shows NDR features already at biases that compare to 200 mV per period with a maximum current of 22 kA/cm^2. The features of an early NDR is also observed by Gajić *et al.* where the maximum current is however lower, at 8 kA/cm^2. Both results differ from our findings and experimental observations. The linear increase in gain with respect to Fd, below saturation, see Fig. 3, is also reported by Bai *et al.*. The output is estimated by both groups and their results are in the range of 300-400 mW, showing a larger discrepancy with experiment than our results.

4. Second harmonic generation

The current at the second harmonic is given by the terms J_2^{cos} and J_2^{sin} in Eq. (1), which are generated by our simulations if $n_{max} \geq 2$ is used. Its total amplitude $|J_2| = ((J_2^{cos})^2 + (J_2^{sin})^2)^{1/2}$ is plotted versus ac field strength in Fig. 5 for different dc bias points. As expected for the process of SH generation, the second order current in the inset of Fig. 5 shows a quadratic behavior for small ac field strengths. The convergence of the higher order terms in Eq. (1) with respect to n_{max} can also be studied in Fig. 5. Here calculations with $n_{max} = 3$ and $n_{max} = 4$ are compared for the bias of 230 mV per period. As seen, the inclusion of four-photon-processes slightly affects the result, especially at high ac field strengths. However, the main features are not changed (this is true for all bias points) and the values are very similar, which is the reason that the computationally lighter simulations with $n_{max} = 3$ were used to calculate the mainstay of the results.

In order to estimate the power emitted at the second harmonic, the waveguide is considered isotropic in the direction transverse to both the growth direction and the propagation direction of the laser field. The second order current response is then assumed to be modulated by the
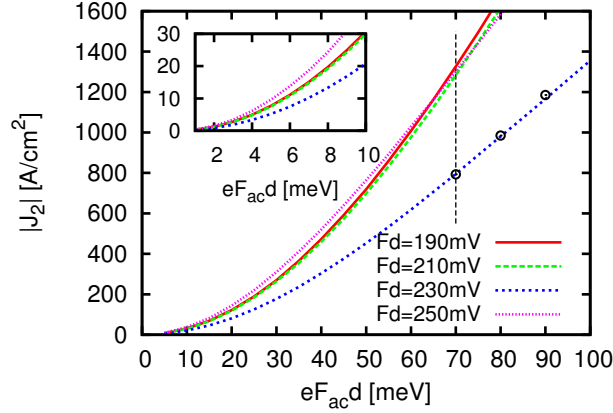
Fig. 5. Current oscillations $|J_2| = ((J_2^{\cos})^2 + (J_2^{\sin})^2)^{1/2}$, at the second harmonic frequency plotted versus ac field strength for the bias points indicated in Fig. 2. Simulations were made with $n_{\max} = 3$. The points inserted along the 230 mV data are results with $n_{\max} = 4$ in order to verify the convergence. Along $eF_{ac}d = 70$ meV there is a dashed line indicating the region studied in more detail in Fig. 6. The inset shows a close-up on small values of the ac field strength, emphasizing the quadratic behavior.

intensity of the traveling wave, used for the linear power, at the fundamental frequency. Through the Helmholtz equation the vector potential generated by this oscillating current density can be calculated and related to a field propagating in the waveguide. Losses and the mismatch in wavevector k for the fundamental and second harmonic frequency are then naturally taken into account. A sketch of this derivation can be found in the Appendix. The resulting equation relates the intensity and the second order current response as

$$I_{2\omega} = \frac{\mu_0 |J_2|^2 c}{8 n_{2\omega}} \left| \frac{1 - e^{-k_{2\omega}'' L} e^{i\Delta k L}}{\Delta k + i k_{2\omega}''} \right|^2 \tag{3}$$

where μ_0 is the magnetic permeability, c the speed of light, n_ω the refractive index at frequency ω, L is the length of the cavity, Δk is the mismatch defined by $\Re\{k_{2\omega}\} - 2k_\omega$, $k_{2\omega}'' = \Im\{k_{2\omega}\}$ is the waveguide attenuation at 2ω. Equation (3) is similar to Eq. (13) of [15], where it was pointed out that Δk dominates over $k_{2\omega}''$. By achieving true phase matching and thus drastically decreasing the k-mismatch, Malis *et al.* [38] was able to increase the conversion efficiency almost three orders of magnitude compared to [15]. For the bias point of $Fd = 215$ mV and the ac field strength of 82 meV, corresponding to the maximum experimental current and the value $eF_{ac}d$ which saturates the gain to the level of the losses, the second order current response is

case:	TW	SW	Exp. res.
I_ω	280 mW	140 mW	100 mW
$I_{2\omega}$	6.0 μW	1.5 μW	550 nW

Table 1. Intensities for the different waveguide models outside the waveguide. These are calculated for a transmission coefficient of 71%. For comparison the experimental results from [15] are shown.
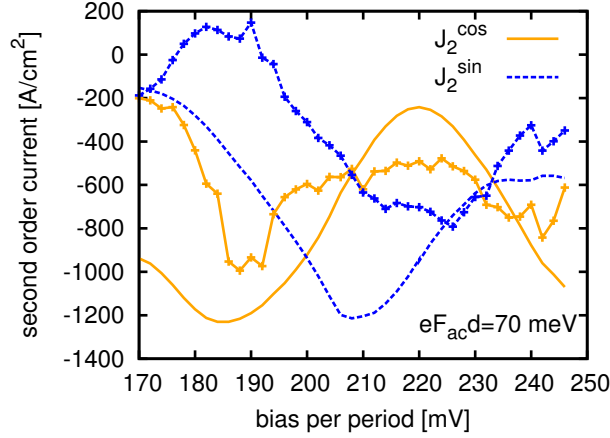
Fig. 6. Current response at 2ω in terms of the cosine and sine part respectively, from the NEGF model (solid lines). These are compared with the results from Eq. (5) using occupations and dipole matrix elements from our nonequilibrium states (connected dots). To compare directly to Eq. 4, the negative particle current, appropriate for electrons, is shown. The ac field strength is held constant at $eF_{ac}d = 70$ meV.

about $|J_2| \approx 1450$ A/cm^2. Using Eq. (3) this would generate an intensity of $I_{2\omega} = 260$ nW/μm^2 inside the waveguide yielding, including Fresnel losses, a total power outside the facet of 6.0 μW. The parameters of [15] were used, with a refractive index of $n_{2\omega} = 3.35$, an attenuation of $k''_{2\omega} = 3$ cm^{-1} together with a sample length of $L = 2.25$ mm. Here as well, the reduction in output power due to additional saturation from the back reflected wave should be taken into account. For a SW, the factor of one half enters the SH intensity squared, giving a reduction of 25% compared to a TW. All results are summarized in Table 1.

Compared to the calculations of Bai *et al.* and Gajić *et al.* which yielded powers of 90 μW and 45 μW respectively, our findings are significantly closer to the experimental results, where the maximum SH output power was reported to be 550 nW in total. As the mode structure in the waveguide is not taken into account in the calculation, it is expected to overestimate the experimental value. Although the quantitative agreement of the SH power is not perfect, the final estimation of the second harmonic signal so close to the experimental value should still be regarded as a good indication towards the validity of the approach and the robustness of the finite-intensity-model that we have applied to the problem.

5. Density matrix calculation

The benefit from our approach described above is that the current response at 2ω can be related directly to the coherences in the density matrix between the different states in the SH generating ladder. Often these coherences are approximated using the difference in populations, i.e. the diagonal elements in the density matrix, and the widths of the transitions. This approach is common when nonlinear conversion is considered [3, 6, 39] and the concept is outlined by both Shen [40] and Boyd [41]. In the following we compare our data with the standard density matrix approach of calculating the second order susceptibility. Using the definition $P(t) = \varepsilon_0 \sum_{\omega_i} \chi(2\omega_i) E^2(\omega_i) e^{-i2\omega_i t}$ (negative frequencies allowed) the current at 2ω can

be expressed as

$$J(t) = \dot{P}(t) = -\omega \varepsilon_0 F_{\text{ac}}^2 \left[\Re\{\chi^{(2)}(2\omega)\} \sin(2\omega t) \right.$$
$$\left. - \Im\{\chi^{(2)}(2\omega)\} \cos(2\omega t) \right] \quad (4)$$

where F_{ac} enters the classical driving field as $E(\pm\omega) = F_{\text{ac}}/2$ and the susceptibility $\chi^{(2)}$ is calculated following Boyd [41] from

$$\chi^{(2)}(2\omega) = -\frac{e^3}{\hbar^2 d\varepsilon_0} \sum_{mnv}$$
$$\frac{(n_m - n_v) \cdot z_{mn} z_{nv} z_{vm}}{(\omega_{nm} - 2\omega - i\gamma_{nm})(\omega_{vm} - \omega - i\gamma_{vm})}$$
$$-\frac{(n_v - n_n) \cdot z_{mn} z_{vm} z_{nv}}{(\omega_{nm} - 2\omega - i\gamma_{nm})(\omega_{nv} - \omega - i\gamma_{nv})} \quad (5)$$

where the populations n_i are sheet densities and z are the dipole matrix elements. In order to use this formula we use the electron densities and states of our simulations. Our system Hamiltonian is rediagonalized using the information of the already converged self-energies. This way the Wannier-Stark states are found, giving an adequate description of the energy eigenstates at the given bias point. The values for the level differences ω_{ij}, occupations, and dipole matrix elements are then extracted from these eigenstates, whereas the broadenings Γ_i are extracted from the self-energies. The values of γ_{ij} in Eq. (5) are the widths of the transitions and this is taken to be $\gamma_{ij} = (\Gamma_i + \Gamma_j)/4$ which is half of the mean. This is done in order to take correlation effects [42] into account phenomenologically.

The result from this calculation is shown alongside the simulation results of the NEGF model in Fig. 6. Results are shown for a large range of bias points, although experimental studies most likely do not reach beyond biases of 215 mV per period as discussed above. The calculations via Eq. (5) show the same magnitude and general trends as the full simulations, although the behavior appears erratic and shows a lot of jitter. Moreover the simulations show a large dip in conversion efficiency around the bias point of $Fd = 230$ mV, also visible in Fig. 5. In the density matrix calculation this is heavily damped, which indicates that the full model, where also higher than second order parts are included, shows additional features not pursueable with ordinary population- and rate-based calculations. It is our belief that these effects are better described in the full model as the nonlinear current response is directly extracted from the off-diagonal density matrix elements, i.e. the coherences in the system.

6. Conclusion

We reported microscopic simulations within our NEGF model for the sample of [15]. Using nominal sample parameters, our results for the threshold current and the lasing power agree well with experimental data. Having a full description of the physical state under operation, our model also provides higher harmonics in the output. The intensity obtained for second harmonic generation is comparable with experimental data. As earlier calculations with simplified models were more of qualitative nature, this demonstrates the necessity of a more detailed model, such as the one used here. The second harmonic generation is compared with a common expression for the second-order susceptibility, which reproduces the full numerical results qualitatively, but shows some deviations and jitter due to the neglect of coherences.

Appendix

In this section we discuss Eq. (3), used to compare the current response to the generated intensity in the waveguide. Both phase matching and absorption in the waveguide is included in the expression, yielding a simple though reasonable estimate of the intensity due to the current response function.

Waveguide models

In the simulations a local field $F(t) = F_{dc} + F_{ac}\cos(\omega t)$ is assumed. If the electric field has a phase shift φ, this corresponds to a local shift in time to $t' = t - \varphi/\omega$ and the current response is

$$J(t) = J_0 + \Re\{J_1 e^{-i(\omega t - \varphi)} + J_2 e^{-i(2\omega t - 2\varphi)}\} \quad \text{for} \quad F(t) = F_{dc} + F_{ac}\cos(\omega t - \varphi). \quad (6)$$

In the waveguide a traveling wave has the form

$$F_0 \cos(k_\omega x - \omega t) \quad (7)$$

where $k_\omega = n_\omega \omega/c$ is approximately real, as absorption and gain compensate (this is not entirely true, as the absorption contains waveguide losses). This wave has the intensity given by the time-averaged Poynting vector

$$\mathbf{S} = F_0^2 \frac{n_\omega c \varepsilon_0}{2} \mathbf{e}_x$$

which is then subject to reflection and transmission when it reaches the facet at the end of the waveguide.

Second harmonic generation neglecting reflecting wave

Without the reflecting wave, we have the local field (7) and we can apply Eq. (6) with the phase shift $\varphi = k_\omega x$. Thus we can identify

$$F_0 = F_{ac,0}$$

where $F_{ac,0}$ is the ac field strength of a traveling wave in balance with the gain medium. This simple equality would not hold for a standing wave, as the back reflected wave would increase the gain saturation.

Assuming a second order current distribution

$$\mathbf{J}_{sh}(x,t) = \Re\{\tilde{J}_{sh}(x) e^{-2i\omega t}\} \mathbf{e}_z$$

within the one-dimensional waveguide between $x = 0$, and $x = L$, where the complex current $\tilde{J}_{sh}(x) = J_2 e^{i2k_\omega x}$ can be found from inspection of Eq. (6). Next we evaluate the electromagnetic field radiated from this current distribution. We consider the Helmholtz equation for the z-component of the vector potential A_z at a frequency 2ω

$$\frac{\partial^2}{\partial x^2} A_z(x, 2\omega) + k_{2\omega}^2 A_z(x, 2\omega) = -\mu_0 \tilde{J}_{sh}(x)$$

where $k_{2\omega}$ is the complex wavevector at frequency 2ω in the waveguide. With the outgoing Green's function $i e^{ik_{2\omega}|x-x'|}/(2k_{2\omega})$ the solution for the Helmholtz equation reads for $x \geq L$

$$A_z(x, 2\omega) = \int_0^L dx' \mu_0 \tilde{J}_{sh}(x') \frac{i}{2k_{2\omega}} e^{ik_{2\omega}(x-x')}. \quad (8)$$

For a given vector potential $\Re\left\{\mathbf{e_z}A_0e^{i(k_{2\omega}(x-L)-2\omega t)}\right\}$ we obtain the time-averaged Poynting vector $\mathbf{P}$ within a standard calculation as

$$\mathbf{P} = |A_0|^2\frac{\omega\Re\{k_{2\omega}\}}{\mu_0}e^{-2k_{2\omega}''(x-L)}\mathbf{e_x} \tag{9}$$

where $k_{2\omega}'' = \Im\{k_{2\omega}\}$ is the waveguide attenuation at the second harmonic. Inserting A_0 from Eq. (8) will yield Eq. (3) with $x = L$ and assuming that $\Re\{k_{2\omega}\} >> \Im\{k_{2\omega}\}$ holds.

Acknowledgments